Growth, domain structure, and atomic adsorption sites of hBN on the Ni(111) surface

Miriam Raths , 1,2,3,* Christina Schott, 4,* Johannes Knippertz, 4 Markus Franke, 1,2 You-Ron Lin , 1,2,3 Anja Haags , 1,2,3 Martin Aeschlimann, 4 Christian Kumpf , 1,2,3,† and Benjamin Stadtmüller , \$\omega^{4,5,\ddagger}\$ ¹Peter Grünberg Institut (PGI-3), Forschungszentrum Jülich, 52425 Jülich, Germany ² Jülich Aachen Research Alliance (JARA) – Fundamentals of Future Information Technology, 52425 Jülich, Germany ³Experimentalphysik IV A, RWTH Aachen University, Otto-Blumenthal-Straße, 52074 Aachen, Germany ⁴Department of Physics and Research Center OPTIMAS, University of Kaiserslautern, Erwin-Schroedinger-Strasse 46, 67663 Kaiserslautern, Germany

⁵Institute of Physics, Johannes Gutenberg University Mainz, Staudingerweg 7, 55128 Mainz, Germany



(Received 1 July 2021; accepted 27 August 2021; published 17 September 2021)

One of the most important functionalities of the atomically thin insulator hexagonal boron nitride (hBN) is its ability to chemically and electronically decouple functional materials from highly reactive surfaces. It is therefore of utmost importance to uncover its structural properties on surfaces on an atomic and mesoscopic length scale. In this paper, we quantify the relative coverages of structurally different domains of a hBN layer on the Ni(111) surface using low-energy electron microscopy and the normal incidence x-ray standing wave technique. We find that hBN nucleates on defect sites of the Ni(111) surface and predominantly grows in two epitaxial domains that are rotated by 60° with respect to each other. The two domains reveal identical adsorption heights, indicating a similar chemical interaction strength with the Ni(111) surface. The different azimuthal orientations of these domains originate from different adsorption sites of N and B. We demonstrate that the majority (\approx 70%) of hBN domains exhibit a (N, B) = (top, fcc) adsorption site configuration while the minority $(\approx 30\%)$ show a (N, B) = (top, hcp) configuration. Our study hence underlines the crucial role of the atomic adsorption configuration in the mesoscopic domain structures of in situ fabricated two-dimensional materials on highly reactive surfaces.

DOI: 10.1103/PhysRevMaterials.5.094001

I. INTRODUCTION

One of the great challenges in information technology is to develop novel concepts and materials for the realization of active functional units on ever-smaller length scales down to the nanoscale or even the single-layer limit [1-3]. The most straightforward way to implement such nanoscale assemblies is to employ intrinsic two-dimensional (2D) materials such as atomically thin honeycomb materials [4–8] or transition metal dichalcogenides (TMDs) [9–11]. These types of materials reveal exceptional optical and spin-dependent electronic properties in their freestanding form. They can also host Dirac fermions with exceptional Fermi velocities [12] or exhibit spin- and valley-dependent degrees of freedom that dominate the helicity-dependent light absorption of the material [10,13]. On surfaces, however, these unique properties (and many others) are often altered or fully suppressed by the proximity between the 2D material and the surface and the chemical interaction at this interface [14–16].

In this regard, hexagonal boron nitride (hBN) has emerged as an essential member of the family of atomically thin materials and their heterostructures [17–19] since it is a 2D insulator with a large band gap of $\approx 5.5-6.0$ eV [20]. It has already been successfully used as 2D buffer layer to chemically and electrically decouple molecular layers and 2D materials from metal surfaces [21,22]. In addition, hBN is also often selected as a buffer layer due to its structural similarity to graphene. This is an important prerequisite for a (quasi)epitaxial and homogeneous growth of graphene, graphenelike materials, or molecular carbon allotropes on hBN-passivated metal surfaces [23–25].

So far, the structural quality of atomically thin honeycomb and molecular materials on hBN-passivated metal surfaces is still limited by the uniformity and corrugation of the hBN template [25]. In particular, the fabrication of hBN monolayer films on metals by chemical vapor deposition (CVD) does not always result in uniform films as known for graphene, but in small triangular-shaped islands exhibiting differently oriented domains. This complex structure formation is mainly attributed to the site-specific interactions of the boron and nitrogen atoms of the hBN layer with the surface atoms resulting in different possible adsorption sites of B and N on metal surfaces.

One of the most frequently studied hBN/metal model systems is a single-layer hBN on Ni(111). The hBN monolayer film grows in a commensurate 1×1 superstructure on the Ni(111) surface with an almost vanishing vertical corrugation [26–31]. These structural properties of hBN are the result of a strong chemical interaction between the 2D layer and

^{*}These authors contributed equally to this work.

[†]Corresponding author: c.kumpf@fz-juelich.de

[‡]Corresponding author: bstadtmueller@physik.uni-kl.de

the magnetic transition metal surface. The differences in the vertical position of N and B above the Ni surface layer are rather small ($\Delta z_{\rm B,N} \leq 0.15$ Å) and can be attributed to the different adsorption positions of N and B on the Ni(111) surface [26,29]. While N adsorbs on a top site of the Ni(111) surface, B is either located on an fcc or an hcp hollow site, depending on the sample preparation conditions. In addition, nonepitaxial hBN domains were recently uncovered, exhibiting various azimuthal orientations and a significantly weaker interaction between the 2D materials and the surface [32]. This manifold of hBN structures on Ni typically leads to a coexistence of different hBN domains on the same surface, most prominently the two 60°-rotated epitaxial domains that exhibit almost identical adsorption energies [27,33]. Interestingly, the adsorption energy difference of these domains is smaller than the thermal energy during the hBN growth and hence cannot explain the typically larger coverage of one epitaxial domain over the other at submonolayer coverages. It is therefore of crucial importance to obtain a more quantitative understanding of the relative coverages of coexisting hBN domains of in situ fabricated hBN layers on surfaces in order to optimize their mesoscopic domain structure for future applications in device structures.

In this paper, we therefore revisit the structural properties of the *in situ* fabricated hBN domains on Ni(111) on the atomic and mesoscopic scale by combining low-energy electron microscopy (LEEM) and the normal incidence x-ray standing wave (NIXSW) technique. These experimental tools allow us to unambiguously determine the atomic structure of the different hBN domains on Ni(111) and to quantify their relative coverages with high accuracy. We find that structural defects at the Ni surface act as nucleation centers for the epitaxial hBN domains. With time, these domains expand over the entire surface and, when the monolayer coverage is reached, clearly exhibit one majority and one minority domain (in terms of covered surface area). The relative coverages are highly reproducible and only depend on the sample preparation conditions during the hBN film growth.

II. EXPERIMENTAL DETAILS

A. Sample preparation

For both the LEEM and NIXSW experiments, the surface of the Ni(111) single crystal was cleaned by repeated cycles of sputtering with argon ions ($t=60 \, \mathrm{min}$, $E_{\mathrm{ion}}=1 \, \mathrm{keV}$) followed by sample annealing at 870 K for 30 min. Afterwards, hBN was grown by CVD. With the crystal at 850 K, we exposed the surface to the precursor gas borazine (HBNH)₃ at a partial pressure of 1×10^{-8} mbar. With this procedure, an almost closed layer of hBN was achieved after 100 min, which corresponds to a nominal exposure of 48 L. Borazine was provided by Katchem (Prague, Czech Republic) and cooled to temperatures below 270 K at all times in order to minimize thermal degradation.

The quality of the samples used for the NIXSW experiment was verified by microchannel plate low-energy electron diffraction (MCP-LEED) after preparation. The LEEM experiments were performed *in situ* and in real time during the growth. Afterwards these samples were cooled down to room

temperature (RT) for further investigation by micro-LEED (μ LEED) and LEEM.

B. Low-energy electron microscopy

The growth study of hBN on Ni(111) was performed using an aberration-corrected low-energy electron microscope (Elmitec AC-LEEM 3). In different imaging modes the microscope can reach a maximal lateral resolution of 2 nm. By switching to diffraction mode, the microscope allows us to obtain LEED patterns from selected surface areas with diameters down to 250 nm (μ LEED). From a LEED pattern, specific beams can be selected for imaging by positioning a contrast aperture in a suitable diffraction plane in the microscope's optics. When the specular (00) beam is selected, the microscope is being operated in bright-field (BF) LEEM mode. Contrast between different surface regions is then produced by, e.g., different surface terminations or stoichiometries and can be tuned by adjusting the interaction energy (the so-called start voltage). Also, LEEM-intensity-vs-start-voltage [LEEM-I(V)] curves can be recorded. In the so-called dark-field (DF) LEEM mode, a non-zeroth-order reflection is selected for imaging. Only surface areas having a specific crystalline structure become visible in this mode, and can be distinguish from other areas that have different structures. This also allows one to distinguish between (e.g., rotational) domains of the same structure on the surface.

In our LEEM experiment, we investigated the growth of the first hBN layer on Ni(111) in situ and in real time. The pressure during these experiments was $\leq 10^{-10}$ mbar and $\approx 1 \times 10^{-8}$ mbar during growth (see above). All LEEM images were collected using start voltages up to $U_{\text{start}} = 25 \text{ V}$, except for the dark-field images, for which we used $U_{\text{start}} =$ 60 V. No electron-beam-induced damage of the hBN films was observed in our LEEM experiments. Note that the focal length of the objective lens can be tuned in order to optimize the imaging. Underfocusing (that is, using a focal length longer than the actual distance between the sample and the objective lens) and strong overfocusing (focal length clearly shorter than the distance to the sample) allow us to identify very small objects on the surface, such as, e.g., nuclei in the very first stage, since these objects appear blurry and their size is strongly overestimated. The sharpest images showing the objects most realistically in size are in turn usually obtained when the image is slightly overfocused, close to in-focus conditions.

C. Normal incidence x-ray standing waves

The normal incidence x-ray standing wave (NIXSW) experiments were carried out at the hard x-ray photoemission (HAXPES) and x-ray standing wave (XSW) end station of beamline I09 at the Diamond Light Source (Didcot, UK). This end station is equipped with a hemispherical electron analyzer (Scienta EW4000 HAXPES) that is mounted perpendicular to the incoming photon beam. The angular acceptance of the electron analyzer is $\pm 30^{\circ}$.

The NIXSW method allows one to determine the vertical adsorption position of all chemically different atomic species within an adsorbate system above the surface with a very high precision, better than 0.04 Å. Here, the fundamental aspects of this method are briefly summarized. For a more detailed introduction we refer the reader to more detailed articles [34,35].

If an incident synchrotron beam fulfills the Bragg condition $\vec{k}_H - \vec{k}_0 = \vec{H}$ for the reflection $\vec{H} = (hkl)$ of the substrate crystal, an x-ray standing wave field is formed by the coherent superposition of the incoming and the Bragg-reflected wave. Scanning the photon energy E through the Bragg condition results in a shift of the phase difference $\Phi(E)$ between the relative complex amplitudes of the incoming and Bragg reflected waves by π . As a consequence, the standing wave field shifts through the crystal by half of the lattice spacing $d_{(hkl)}$ in the direction perpendicular to the Bragg planes. This changes the amplitude of the standing wave at any specific position (height) in and above the crystal, and hence also the x-ray absorption of an atom that is located at this position. This change in the absorption yield can in turn be measured by recording the photoemission yield I(E) of any of its core levels, as a function of the photon energy. The resulting experimental yield curve I(E) is characteristic for the height of that specific atomic species, with respect to the Bragg planes of the bulk Bragg reflection used. I(E) can be modeled by

$$I(E) = 1 + S_R R(E) + 2|S_I|\sqrt{R(E)} \cdot F^H \cos [\Phi(E) - 2\pi P^H + \psi], \quad (1)$$

where R(E) is the x-ray reflectivity of the Bragg reflection with its complex amplitude $\sqrt{R(E)}$ and phase $\Phi(E)$. S_R and $S_I = |S_I|e^{i\psi}$ are correction parameters for nondipolar contributions to the photoemission yield for emission from an s state [34–36]. The actual fit parameters are the coherent position P^H and the coherent fraction F^H . P^H is the averaged vertical distance of the atomic species to the next (hkl) lattice plane below, in units of the lattice spacing $d_{(hkl)}$ of the corresponding Bragg reflection. Hence the distance (in units of angstrom) between an adsorbate and the surface Bragg plane can be written as $D^H = (P^H + n) \cdot d_{(hkl)}$, with n being the number of Bragg planes located between the surface plane and the adsorbed atoms. In our case, n = 1, since the adsorption heights of B and N turn out to be slightly higher than the lattice spacing $d_{(hkl)}$. F^H can be understood as a vertical order parameter with values between 0 and 1. Small values usually indicate multisite adsorption or even a very broad distribution of adsorption heights, while for $F^H=1$ all emitters are located at the same coherent position P^H . Finally, we want to mention that D^H and P^H give insight into the adsorption heights of a specific species above the surface only when a reflection H perpendicular to the surface is selected. In our case this is the (111) reflection. When an inclined reflection is selected, the measured vertical positions D^H have to be understood as distances to the inclined Bragg planes of that reflection. They reflect the lateral position of the atoms on the surface such as the atomic adsorption site of adsorbates on surfaces.

In our work, we recorded NIXSW data for the (111) Bragg reflection in order to measure the (vertical) adsorption heights above the Ni(111) surface plane of the N and B atoms in the hBN layer, and for the (-111) reflection to determine the (lateral) adsorption sites of both species.

III. RESULTS AND DISCUSSION

A. Growth of hBN on Ni(111)

The growth of hBN on Ni(111) was observed *in situ* and in real time using LEEM. Figure 1 shows exemplary LEEM images at characteristic stages of the hBN growth process. The LEEM image of the clean Ni(111) surface [Fig. 1(a)] reveals the existence of two types of dark objects at the surface: Thin lines represent step edges separating clean Ni terraces, and dark spots that can be attributed to point defects on the surface. The rather large defect density is attributed to the high surface reactivity of the Ni(111) surface and the typical existence of impurity atoms in the Ni bulk material. The size of these defects is strongly enhanced due to the chosen imaging conditions ($U_{\text{start}} = 1.20 \text{ V}$, overfocused).

When introducing borazine into the chamber, the size of the dark spots increases instantaneously as illustrated in Fig. 1(b). This indicates that hBN islands nucleate preferably at defects on the Ni(111) surface. The subsequent growth of hBN is shown in the LEEM images in Figs. 1(c)–1(h). Here the islands appear bright on the dark Ni(111) surface and are imaged in their true lateral size. These images were recorded under different imaging conditions ($U_{\text{start}} = 3.50 \text{ V}$, slightly overfocused), which explains the contrast inversion from Fig. 1(b) to Fig. 1(c).

A closer inspection reveals two different types of hBN islands with different brightness in the LEEM images in Figs. 1(c)–1(h). We will refer to these islands as α (blue arrows) and β islands (orange arrows). Initially, most islands are of the α type appearing brighter than the β islands. This indicates a significantly higher nucleation density of the α islands (compared with β). With time, both types are growing: β islands grow somewhat faster than α islands in this early stage (up to \approx 25 min), but they are also stopped early when their edges touch the numerous α islands around. Hence, in the later growth stage, remaining gaps in the hBN layer are filled with the α domain only, resulting in a clear majority of this domain type when the surface is completely covered after a deposition time of 100 min.

B. Domain structure of the hBN layer

We investigated the closed hBN layer further using BF-LEEM and LEEM-I(V). Figure 2(a) shows an enlarged LEEM image of the same surface region as discussed in Fig. 1, at different imaging conditions ($U_{\text{start}} = 22.5 \text{ V}$) and after cooling the sample to RT. At this start voltage, *three* island types with different LEEM intensity can be observed. Around the two small β islands (one of them is marked with an orange arrow) we can identify regions at two significantly different brightness levels. A comparison with Fig. 1(h) indicates that the α regions in fact consist of two different domains, which we refer to as α_1 (blue arrow) and α_2 (cyan arrow) in the following.

Furthermore, we recorded LEEM-I(V) curves for all three types of hBN domains in the voltage range up to $U_{\rm start}=25$ V; see Fig. 2(b). The plateau at negative values is caused by total reflection of electrons at the sample surface. With increasing $U_{\rm start}$, the LEEM intensity decreases significantly. The position of the steep intensity drop close to $U_{\rm start}=0$ reflects

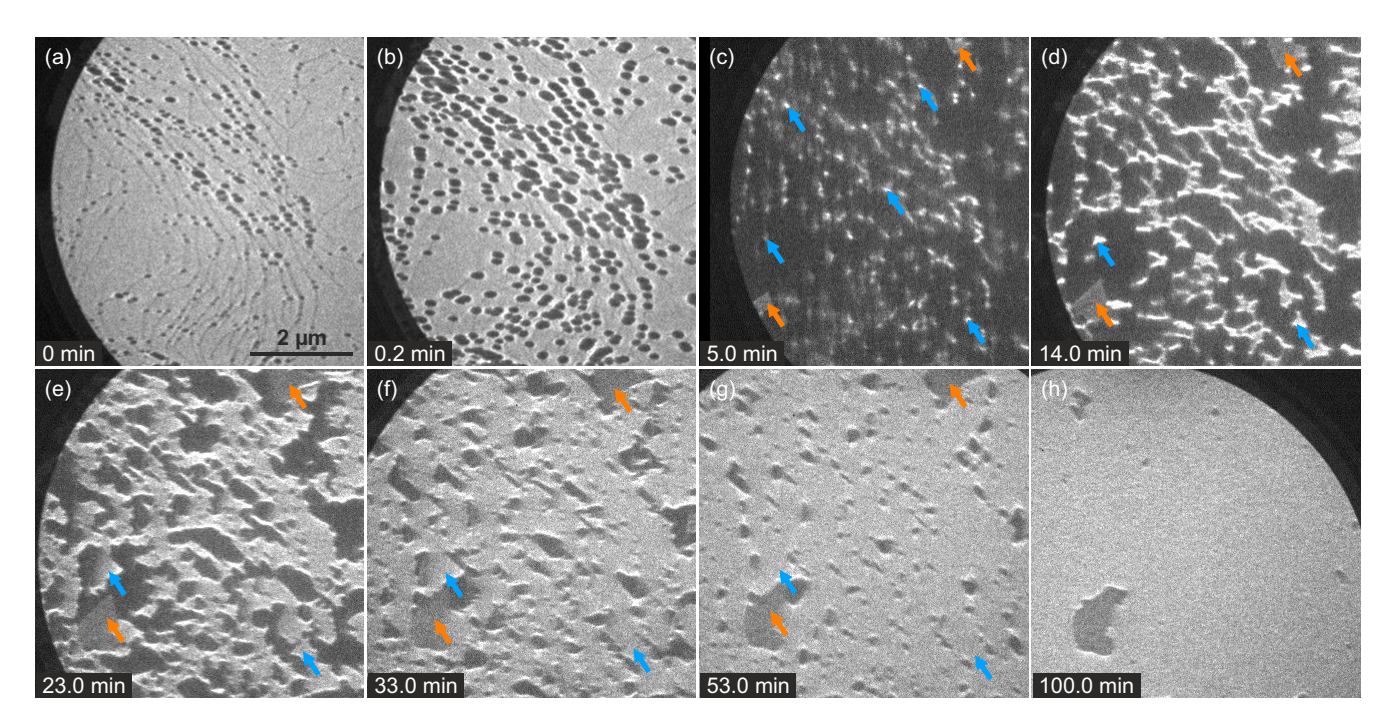


FIG. 1. LEEM images recorded during the growth of hBN on Ni(111) at 850 K and a borazine partial pressure of 1×10^{-8} mbar. (a) LEEM image of the clean Ni(111) surface. (b) Nucleation of hBN at defect sites that appear dark on a bright Ni(111) surface (overfocused, $U_{\text{start}} = 1.20 \text{ V}$). (c)–(h) Growth of two types of hBN islands α and β (blue and orange arrows, respectively) on the dark Ni(111) surface. The α islands are clearly dominant at higher coverage (slightly overfocused, $U_{\text{start}} = 3.50 \text{ V}$, total deposition time $t_{\text{depos}} = 100.0 \text{ min}$).

the (local) work function of the observed surface region. Taking 90% of the maximum intensity as the criterion, Fig. 2(b) reveals that hBN reduces the work function by 0.8 eV for the β region and by 1.7 eV for both α regions with respect to the clean Ni(111) surface (black curve).

In the entire energy range, the LEEM-I(V) curves of the α_1 and α_2 regions are very similar. In particular, minima and maxima of the two curves are located at exactly the same start voltages. Intensities also differ only slightly, most strongly at $U_{\text{start}} = 22.5 \text{ V}$, the energy we used for recording the image shown in Fig. 2(a). The LEEM-I(V) curve for the β region,

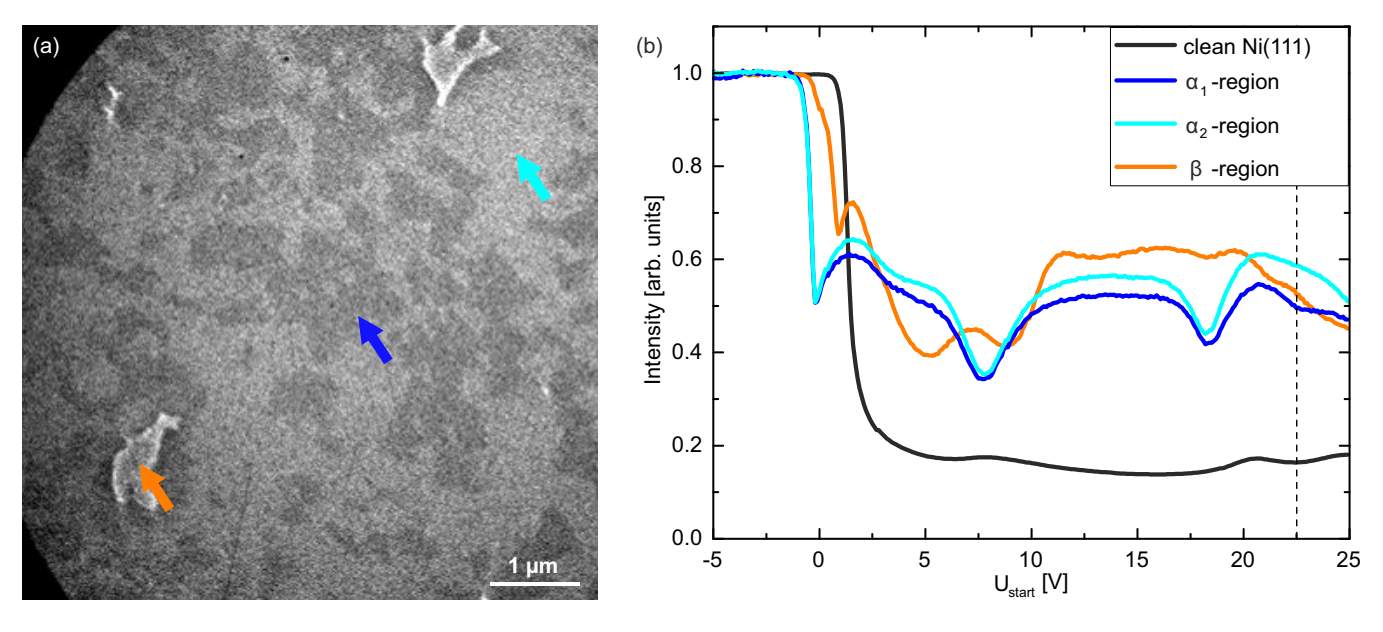


FIG. 2. (a) LEEM image of the same region as shown in Fig. 1, recorded at $U_{\text{start}} = 22.5$ V. Two different α regions (α_1 and α_2 , cyan and blue arrows, respectively) can be distinguished. The β islands appear bright here, in contrast to Figs. 1(c)-1(h). (b) LEEM-I(V) curves recorded on the three types of hBN domains [color code as in (a)] and on the clean Ni(111) surface (black curve). The dashed line marks the start energy used in (a), which produces the best contrast between the α_1 and α_2 regions.

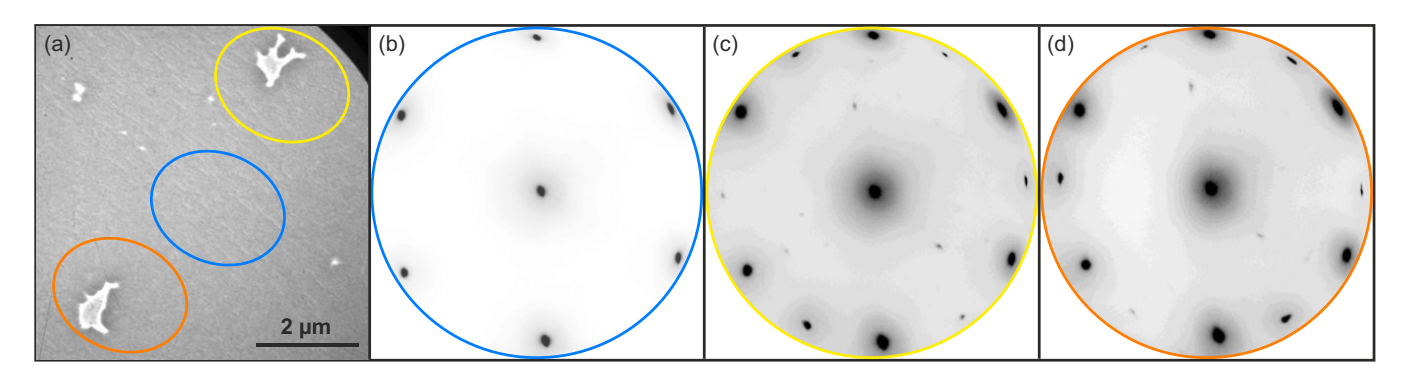


FIG. 3. (a) Close-up of a BF-LEEM image showing two β islands (bright), embedded in a region covered by α_1 and α_2 islands (dark, with small contrast). $U_{\text{start}} = 1.9 \text{ V}$. (b)–(d) μ LEED patterns recorded from the surface areas indicated in (a) by blue, yellow, and orange ellipses, respectively. $U_{\text{start}} = 60 \text{ V}$.

however, has a different shape, and characteristic maxima and minima are located at different start voltages than for the α regions. This, as well as the clear difference in the work functions, indicates structural differences between the α and β regions, most likely caused by different adsorbate-substrate interactions in the two domains [32].

 μ LEED experiments can provide additional insights into the structural differences between α and β domains. By inserting an aperture into the sector field, we selected the surface regions marked by colored ellipses in the LEEM image shown in Fig. 3(a) (diameter $\approx 2 \mu m$). The corresponding diffraction patterns are displayed in Figs. 3(b)-3(d). At first, we focus on the α region [blue ellipse in Fig. 3(a) and LEED pattern in Fig. 3(b); α_1 and α_2 domains cannot be individually selected with this aperture]. In the LEED pattern, no other spots besides the Ni(111) substrate spots are visible; the hBN diffraction spots coincide (within the k-space resolution of our LEEM instrument) with the substrate spots, since the lattice mismatch between the hBN unit mesh and the Ni(111) surface unit mesh is very small. This indicates very clearly that the α domains are well aligned with the substrate lattice and they represent epitaxial hBN-R0° domains (where R0° refers to a rotation of 0°).

In contrast, the μ LEED patterns of the β -type islands reveal additional superstructure spots [besides the Ni(111) bulk spots], as can be seen in Figs. 3(c) and 3(d). The two different islands marked by yellow and orange ellipses in Fig. 3(a) both show a hexagonal pattern of additional LEED spots at the same k_{\parallel} as the bulk spots. With respect to the Ni(111) spots, they are rotated clockwise by 27° and 34°, respectively. We conclude that the β domains are structurally identical to the α domains but are rotated with respect to the bulk lattice; they are *nonepitaxial*, hBN-R ξ domains with variable rotation angle ξ . Note that some additional, weaker diffraction spots at smaller k_{\parallel} are visible, which can be explained by multiple-scattering effects [32].

Finally, we performed DF-LEEM measurements in order to reveal the structural differences between the α_1 and α_2 regions. In Fig. 4 we present five DF-LEEM images [Figs. 4(b)–4(f)] that were recorded by selecting different diffraction spots, as indicated by the numbers and letters in Fig. 4(a). The relevant reflections for studying the α_1 and α_2 regions are labeled 1, 3, 5 and 2, 4, 6, and the DF-LEEM images corresponding to spots 1 (α_1 region) and 2 (α_2 region)

are depicted in Figs. 4(b) and 4(c), respectively. It is obvious that for the (dominant) α regions the dark-gray-light-gray contrast in the images is inverted in Figs. 4(b) and 4(c), while the β domains appear black in both images, as indicated by orange arrows. Very similar to the case of hBN/Cu(111) [37], the contrast inversion can be explained by assuming two symmetrically equivalent hBN domains being rotated by 60° with respect to each other, i.e., oriented 0° and 60° with respect to the Ni(111) substrate. As discussed in detail by Felter et al. (supplement of Ref. [37]), the contrast between the two domains in DF-LEEM originates from the threefold symmetry of the hBN structure, i.e., from the nonequivalence of the hBN {10} and {01} reflections. For 60°-rotated domains, the first group of LEED spots (1, 3, and 5) contains the {10} diffraction spot of one (e.g., α_1) and the {01} spot of the other (α_2) domain, whereas for the other group of LEED spots (2, 4, and 6) it is the other way around. Hence, depending on whether the {10} or the {01} beams are more intense for the electron energy used, the DF image will show either the α_1 or the α_2 domain brighter than the other.

We have also selected the diffraction spots of the β domains for DF-LEEM imaging. Three such spots are marked in Fig. 4(a), located on the arc between the bulk spots and labeled by A, B, and C. Relative to the α -domain spots, these spots are rotated clockwise by $\xi = 27^{\circ}$, 34°, and 41°, respectively. Each of the corresponding DF-LEEM images shown in Figs. 4(d)–4(f) exhibits bright contrast for one single β island, while all the rest of the surface is dark.

Our DF-LEEM results are summarized in the false-color composite image shown in Fig. 4(g). The individual DF-LEEM images in Figs. 4(b)–4(f) are colored in their respective color (blue and cyan for the α domains and yellow, orange, and red for the β domains) and superimposed in one image. The resulting composite image shows that the surface is fully covered and all domains have been identified. It also allows us to quantify the surface fractions that are covered by the individual domains: In the investigated part of the sample, which we consider to be representative of this hBN film, we find a clear minority of $\leq 3\%$ for the β domains, while the majority α regions split into \approx 35% α_1 (blue areas) and \approx 65% α_2 (cyan areas) domains. This indicates that the α domains are not equally occupied. Insight into the origin of this asymmetry can be obtained from a closer investigation of the hBN-substrate interaction, for which we performed NIXSW experiments.

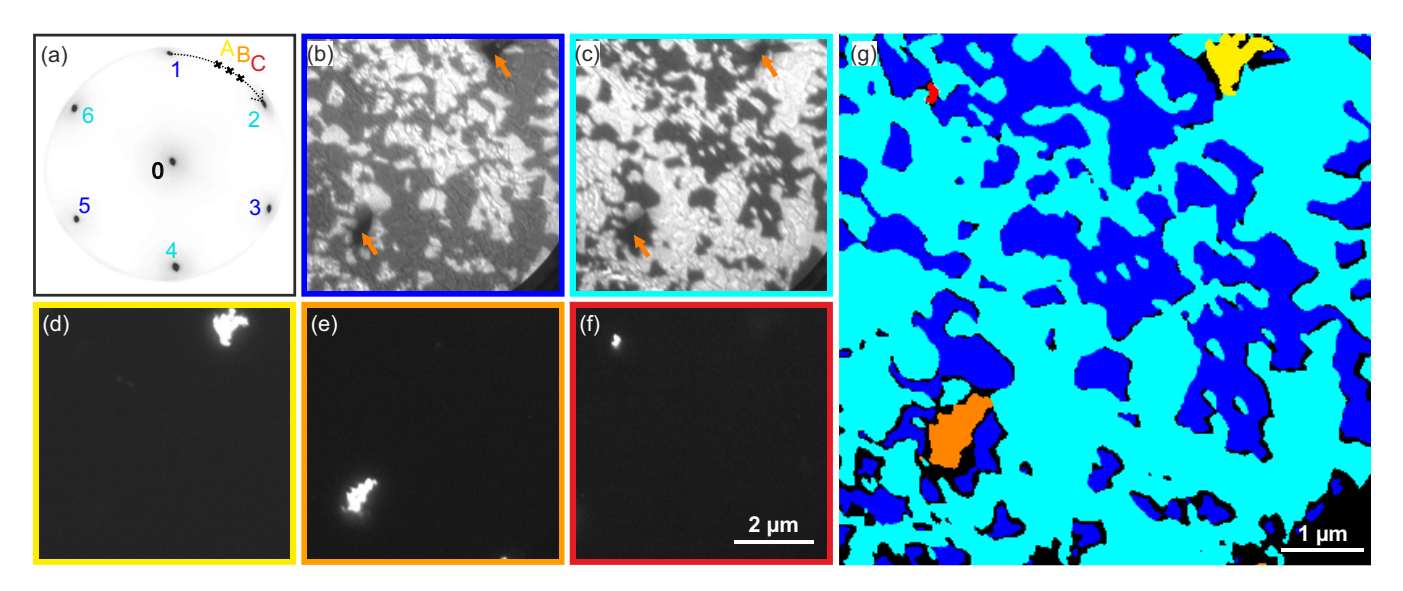


FIG. 4. DF-LEEM study of hBN layer on Ni(111). (a) LEED pattern with all spots used for DF imaging labeled. $U_{\text{start}} = 60 \text{ V}$. (b) and (c) DF-LEEM images recorded for the diffraction spots 1 and 2, showing the two different domains α_1 and α_2 as light- and dark-gray areas. (d)–(f) DF-LEEM images showing three different β domains, corresponding to the spots labeled A, B, and C in (a). The spots are rotated by 27° , 34° , and 41° with respect to spot 1. (g) False-color composite image of all DF images in (b)–(f).

C. Adsorption height and site of hBN on Ni(111)

For our NIXSW experiment, we prepared a new sample at the I09 beamline of the Diamond Light Source using the same growth conditions as in our LEEM experiment. We recorded photoemission-based NIXSW data sets for B and N using the (111) and (-111) Bragg reflections, allowing us to reveal the structural differences between the α_1 and α_2 domains of the hBN film. This was possible since the investigated hBN film consisted of α domains only, i.e., no diffraction spots of β domains were visible in the diffraction pattern of this sample. In the following, we first introduce the spectroscopic signatures of the B 1s and N 1s core levels that are used as photoemission yield signals in the NIXSW experiment. Afterwards, we turn to the NIXSW results for the (111) and (-111) Bragg reflections.

1. Modeling of x-ray photoelectron spectroscopy data

The high-resolution core level spectra of the B 1s and N 1s emission lines were recorded with a photon energy of E = 3000 eV and are shown in Fig. 5. This photon energy is significantly smaller than the Bragg energy and was selected to avoid any influence of the x-ray standing wave field on the spectral line shape. The overall spectral shapes of both core levels are in good agreement with previous experiments [38]. The N 1s spectrum is dominated by a single main line at $E_B =$ 338.7 eV. In contrast, the B 1s spectrum consists of three contributions: an asymmetric main peak at $E_B = 190.6$ eV, a small side peak at $E_B = 189.5$ eV, and a broad electron energy loss tail at larger binding energies. The small side peak of the B 1s spectrum can be assigned to B atoms of residual borazine molecules [39]. In addition, the asymmetric line shape of the B 1s main line is typical for core level signatures of metals and can be attributed to screening and many-body effects in metallic systems [38]. This observation is a first indication of a strong hybridization of hBN π^* and Ni 3d states, and

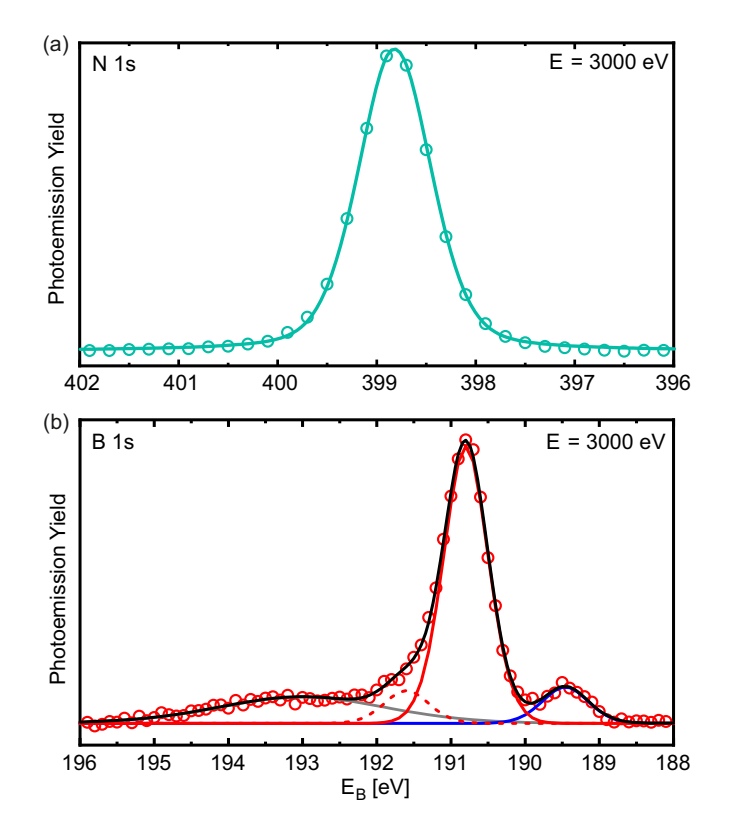


FIG. 5. (a) N 1s and (b) B 1s core level spectra recorded from a monolayer hBN on Ni(111) at a photon energy of E=3000 eV. The experimental data were fitted with Gaussian curves to model the individual contributions. Both spectra show one prominent main peak. The asymmetric line shape in (b) was modeled by two Gaussian curves (red solid and dotted lines). The blue Gaussian curve describes the B 1s signal of borazine residuals. The gray curve indicates the electron energy loss tail.

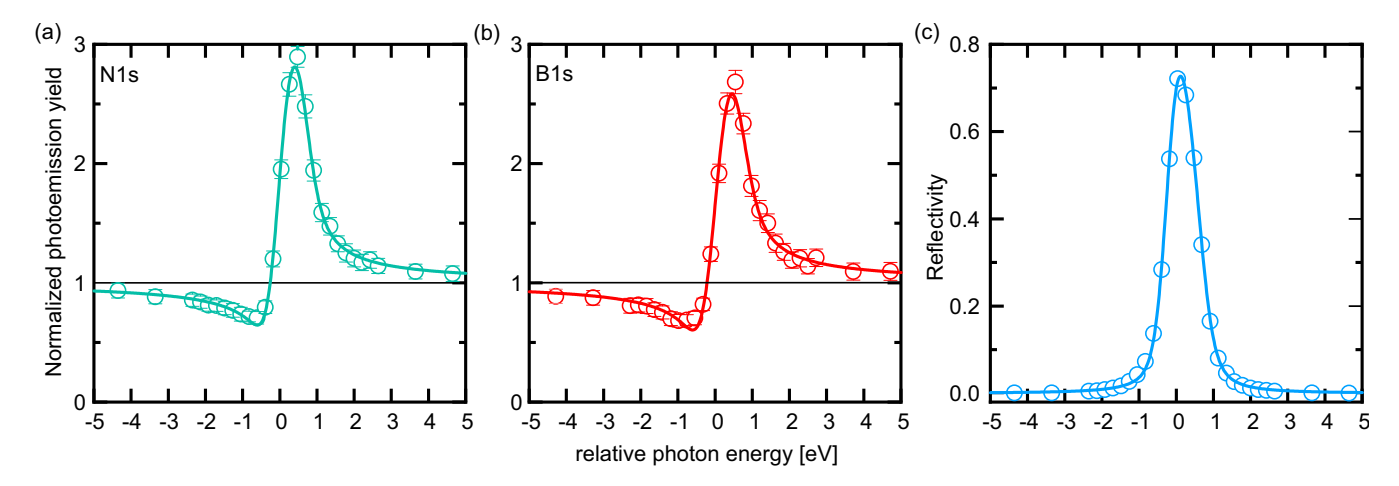


FIG. 6. (a) and (b) NIXSW yield curves of N and B, respectively, for hBN on Ni(111), as extracted from the core level fitting models shown in Fig. 5. (c) X-ray reflectivity curve of the Ni(111) reflection. Measured data points and fitted curves are shown.

hence of a strong (chemical) interaction between hBN and the Ni(111) surface.

For our NIXSW analysis, we model the spectral line shape of these core level data by Gaussian curves. The data analysis was performed using the software CasaXPS [40]. The best fits were obtained for the models shown in Fig. 5. The fitting envelopes are shown as black curves, and the individual components as solid curves of different colors. For B, two Gaussian curves were considered to correctly describe the asymmetric line shape of the B 1s main line [red solid and dotted curves in Fig. 5(b)]. NIXSW yield curves for N and B were extracted from the core level spectra by integrating the fit curves of the main lines.

2. Adsorption height and vertical corrugation

We now turn to the NIXSW results obtained for the (111) reflection, which are the vertical adsorption heights $D^{(111)}$ for B and N. These heights are directly related to the bonding strength between the hBN layer and the Ni(111) surface.

Figure 6 shows typical photoemission yield curves for N 1s and B 1s and the reflectivity curve of the Ni(111) crystal. The uncertainty for each point was estimated by a Monte Carlo error analysis implemented in CasaXPS. The yield curves were analyzed using the NIXSW analysis software TORRICELLI [41,42] considering nondipolar effects in the photoemission process as well as the small deviation of the incidence angle from normal incidence that cannot be avoided in the experiment [36]. NIXSW scans for each species have been recorded on several positions of the sample. The averaged values for the fitting parameters $P^{(111)}$ and $F^{(111)}$ are summarized in Table I.

The coherent fractions for both atomic species are close to unity, $F_N^{(111)} = 1.17(3)$ and $F_B^{(111)} = 1.12(9)$, even exceeding the physically meaningful limit. We attribute this to the nonlinearity of the photoemission detector system of the electron analyzer. This nonlinear behavior is known to occur for large photoelectron count rates, which are well below the saturation threshold of the detector system. It leads to an overestimation of the photoemission yield close to the Bragg energy. Nevertheless, the large coherent fractions indicate the formation of a flat hBN layer on Ni(111) with no significant

difference in the adsorption heights of the two symmetry-equivalent α domains.

The adsorption heights $D^{(111)}$ of B and N are calculated from the coherent positions by $D^{(111)} = (n + P^{(111)}) \cdot d_{(111)}$ with n = 1 and $d_{(111)} = 2.038$ Å; see above. This results in $D_N^{(111)} = 2.28(4)$ Å and $D_B^{(111)} = 2.23(4)$ Å, i.e., in a slightly smaller height for boron than for nitrogen, in agreement with a previous study [26]. Interestingly, the vertical adsorption heights are very close to the covalent bonding distances between both species and Ni (see Table I), indicating a strong bonding and chemical interaction between the hBN layer and the Ni(111) surface.

Our experimental results are in good agreement with previous studies of strongly interacting honeycomb materials on metal surfaces. The strong chemical interaction at the interface between the honeycomb material and the Ni(111) surface leads to epitaxial growth of a layer with marginal vertical buckling and to vertical bonding distances close to covalent bond lengths [26,43]. In particular, we find no indication of a strong vertical buckling of the hBN layer as was observed for hBN on less reactive surfaces such as Ir(111) [44] or Cu(111) [45,46].

TABLE I. Averaged fitting results $F^{(111)}$ and $P^{(111)}$ and corresponding adsorption distances $D^{(111)}$, obtained from the NIXSW analysis of a commensurate monolayer hBN on Ni(111). The nondipolar correction parameters used for the N 1s and B 1s emission lines were $\gamma_{N1s} = 1.124\,86$, $\gamma_{B1s} = 1.196\,41$, $\delta_{N1s} = -0.233\,11$ and $\delta_{B1s} = -0.161\,67$. The experiment was performed at 3.5° off normal incidence, i.e., at a Bragg angle of $\theta = 86.5^\circ$; for details, see Refs. [36,41]. Covalent bonding distances d_{cov} are taken from Ref. [27].

(111)	N 1s	B 1s	
$F^{(111)}$	1.17(3)	1.12(9)	
$P^{(111)}$	0.12(2)	0.09(2)	
$D^{(111)}$ (Å)	2.28(4)	2.23(4)	
d_{cov} (Å)	1.95	2.08	

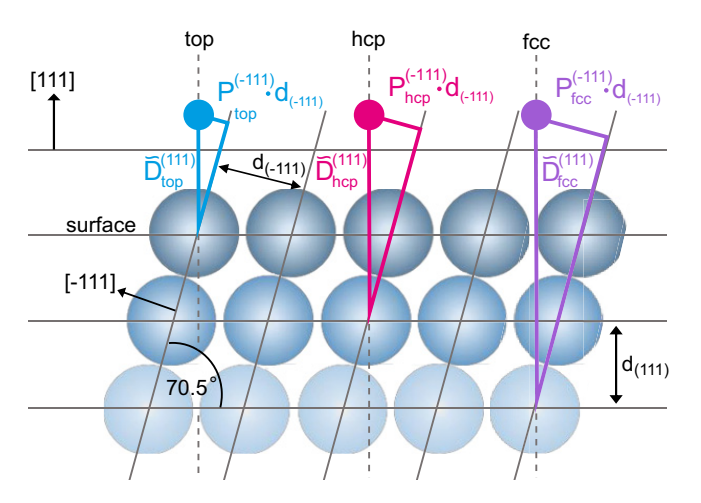


FIG. 7. Illustration of the adsorption geometry for adatoms on the threefold-symmetric sites. Atoms (irrespective of the chemical species) are drawn as cyan, magenta, and purple spheres on the top, hcp hollow, and fcc hollow sites, respectively, at the correct height $D^{(111)}$ above the surface, according to the (111)-based NIXSW experiment. Gray horizontal and inclined lines indicate the (111) and (-111) Bragg planes, respectively, which are tilted by 70.5° with respect to each other. Colored triangles illustrate the trigonometric relation used for calculating the coherent positions with respect to the inclined Bragg planes $P_i^{(-111)}$, where i indicates the top, hcp hollow, and fcc hollow sites.

3. Atomic adsorption sites of N and B

To determine the adsorption sites of N and B, we have performed NIXSW measurements using the (-111) reflection of the Ni crystal. The corresponding Bragg planes are tilted by 70.5° with respect to the (111) surface and hence allow us to obtain *lateral* structural information in this measurement. In particular, every threefold-symmetric adsorption site has its characteristic and unambiguous coherent position $P_i^{(-111)}$ that allows us to identify the adsorption sites of both atomic species unambiguously.

The expected coherent positions in the (-111) NIXSW experiment can be calculated by simple trigonometry. As illustrated in Fig. 7, an adsorbate atom on a top site, an hcp hollow site, and an fcc hollow site is located precisely above a Ni atom of the *first* (cyan), *second* (magenta), and *third* (purple) Ni layer, respectively. The distance of the adsorbate to these Ni atoms is therefore

$$\tilde{D}_i^{(111)} = D^{(111)} + (n_i - 1) \cdot d_{(111)} = (n_i + P^{(111)}) \cdot d_{(111)},$$
(2)

where *i* stands for either the top, the hcp hollow, or the fcc hollow site and $n_{\text{top}} = 1$, $n_{\text{hcp}} = 2$, and $n_{\text{fcc}} = 3$.

Assuming that the height of the adsorbate above the surface (that is, $D^{(111)}$ or $P^{(111)}$) is known [e.g., from the NIXSW experiment using the (111) reflection], the expected coherent positions $P_i^{(-111)}$ for the three adsorption sites can be determined by triangulation, as illustrated by the colored triangles in Fig. 7. With $d_{(-111)} = d_{(111)}$ we find

$$P_i^{(-111)} \cdot d_{(111)} = \tilde{D}_i^{(111)} \cdot \sin 19.5^\circ,$$
 (3)

TABLE II. Measured (-111) NIXSW results for hBN on Ni(111) and expected (calculated) coherent positions $P^{(-111)}$ for B and N on top, hcp hollow, and fcc hollow sites. Expected values for B and N are almost identical since the vertical adsorption heights D^{111} are almost identical for the two species.

	(-111)	N 1s	B 1s
Measured	$F^{(-111)}$	0.99(7)	0.69(2)
	$P^{(-111)}$	0.35(2)	0.97(2)
Expected	$P_{\text{top}}^{(-111)}$	0.37(2)	0.37(2)
	$P_{\text{hcp}}^{(-111)}$	0.71(2)	0.70(2)
	$P_{ m top}^{(-111)} \ P_{ m hcp}^{(-111)} \ P_{ m fcc}^{(-111)}$	0.04(2)	0.03(2)

and hence

$$P_i^{(-111)} = (n_i + P^{(111)}) \cdot \sin 19.5^{\circ}. \tag{4}$$

These expected (calculated) $P^{(-111)}$ values for the threefold-symmetric sites, together with the results of the (-111) NIXSW experiment, are listed in Table II and illustrated in an Argand diagram in Fig. 8. In such a diagram, the NIXSW result is drawn as a polar vector with its length and polar angle representing the (measured or calculated)

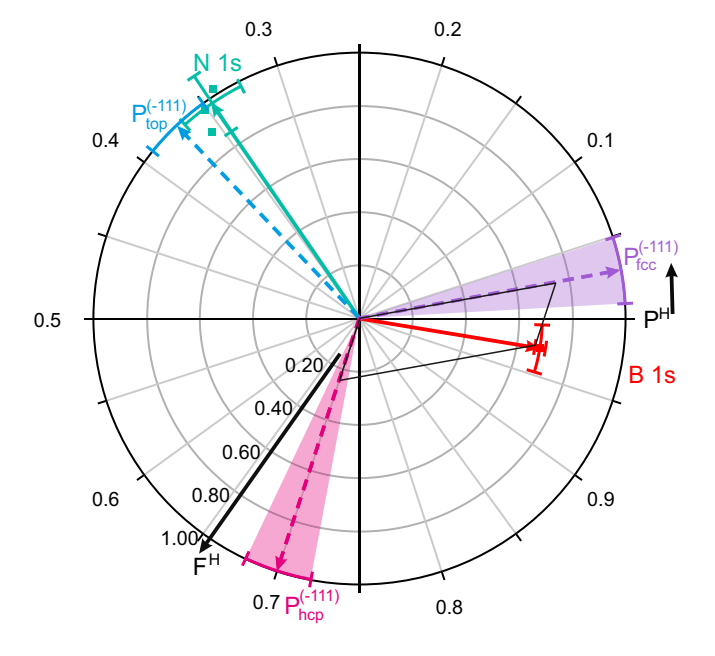


FIG. 8. Argand diagram showing the results and analysis of the (-111) NIXSW experiment. Green and red data points represent the experimental results for N 1s and B 1s, respectively. Cyan, magenta, and purple dashed vectors indicate the expected result for any species adsorbed on top, fcc hollow, and hcp hollow sites, respectively. The error bars for these calculated $P^{(-111)}$ values are obtained from the experimental errors of the corresponding $P^{(111)}$ values (adsorption heights). Hence all possible relative contributions of the hcp and fcc sites to the total vector sum are located in the shaded areas. The black parallelogram illustrates two components of a representative solution of the vector sum equation for the B 1s signal [Eq. (5)] resulting from the statistical analysis based on the experimental confidence interval. This analysis reveals 75(5)% of B atoms occupying fcc hollow sites and 25(5)% on hcp hollow sites.

coherent fraction and position, respectively: $\mathbf{Z} = F^{(-111)} \cdot \exp(2\pi i P^{(-111)})$. Experimental results are shown as green and red data points representing individual NIXSW measurements on different spots on the sample surface. Calculated results for top, hcp hollow, and fcc hollow sites are shown as vectors in the same color as in Fig. 7. The uncertainties of these calculated $P^{(-111)}$ values are included as error bars of identical color. They are based on the experimental uncertainty of the adsorption height D^{111} of B and N above the Ni(111) surface. For all adsorption sites, a coherent fraction of $F^{(-111)} = 1$ was assumed

A comparison of expected and measured values allows us to immediately identify the adsorption site of nitrogen. The measured coherent positions (green data points) match very well with only one of the predicted values, that of the top site. Since the coherent fraction $F_N^{(-111)}$ is almost 1, this must be the case for both domains. Hence we conclude that in both α domains the N atoms are located on top of the uppermost Ni atoms.

For boron the situation is more complicated, because none of the predicted coherent positions is very close to the measured value $P_B^{(-111)}$. Hence (at least) two different adsorption sites must be occupied by the B atoms in the hBN film, which is also reflected by the coherent fraction $F_B^{(-111)}$ being significantly smaller than 1. And indeed, assuming that B occupies both hollow sites, can explain the experimental results very well and is in accordance with the finding that the on-top site is occupied by N. The relative occupation of both hollow sites can be determined by a vector component analysis. The vector \mathbf{Z}_B corresponding to our best fit to the experimental data for B (red data points) can be split into two components, one representing the hcp hollow site and the other representing the fcc hollow site:

$$\mathbf{Z}_{B} = (1 - a) \cdot \mathbf{Z}_{B,\text{hcp}} + a \cdot \mathbf{Z}_{B,\text{fcc}}, \tag{5}$$

where a is the relative occupation of the fcc hollow site by B. To properly quantify the relative occupation a, we performed the vector sum analysis for all possible combinations of $\mathbf{Z}_{B,\text{hcp}}$, $\mathbf{Z}_{B,\text{fcc}}$, and \mathbf{Z}_{B} within their experimental confidence intervals; see Table II. All possible contributions of the hcp and fcc sites to the total vector sum are located in the shaded areas in the Argand diagram in Fig. 8. The black parallelogram illustrates the vector sum analysis for an exemplary data set within the experimental confidence interval. A statistical analysis of all possible vector combinations reveals an average relative occupation of the fcc hollow sites of a = 0.75(5), i.e., approximately three-quarters of B atoms are located on fcc hollow sites while 25(5)% occupy hcp hollow sites.

We hence conclude that the NIXSW technique, just like LEEM, identifies two different hBN domains having an unbalanced occupation of the two types of α domains. We find that in the majority domain (which is the α_2 domain; see above), B occupies an fcc hollow site while N is positioned on a top site, i.e., the α_2 domain has a (N, B) = (top, fcc) adsorption configuration. The minority α_1 domain exhibits a (N, B) = (top, hcp) configuration. The coverage ratios of minority and majority domains determined in both experiments (35%/65% and 25%/75% in LEEM and NIXSW, respectively) agree well with each other, considering that the samples were prepared in

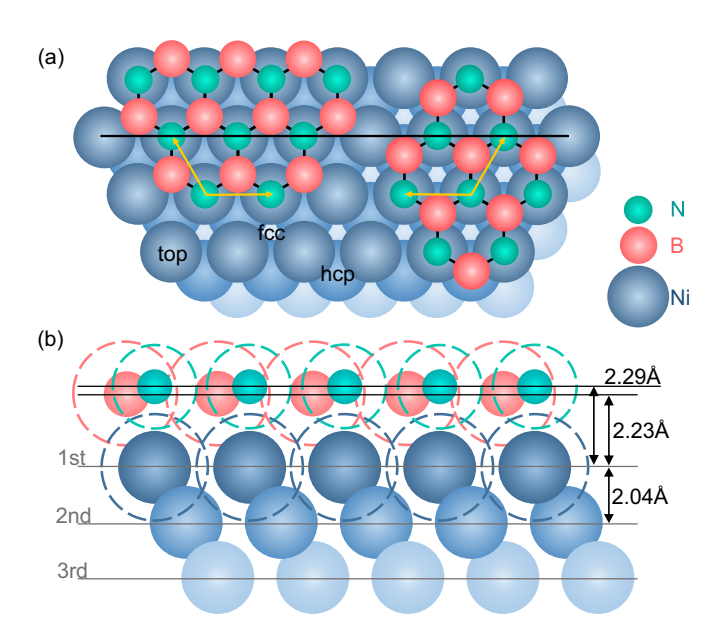


FIG. 9. Adsorption model of hBN on Ni(111) based on the LEEM and NIXSW results. (a) Top view with both adsorption geometries. Left: (N, B) = (top, fcc). Right: (N, B) = (top, hcp). A horizontal solid line indicates a mirror line for mapping one domain onto the other but does not match the Ni bulk symmetry. (b) Truescale vertical adsorption scheme with experimentally determined adsorption heights for nitrogen and boron. The dashed circles indicate the van der Waals radii of every atom. The strong overlap of the circles indicates a strong binding of hBN to Ni(111).

different UHV chambers and different laboratories for the two experiments. As illustrated in the real-space model shown in Fig. 9(a), the two hBN domains are rotated by 60° with respect to each other. Due to the threefold symmetry of the substrate, this implies that the domains are also mirror symmetric, but the mirror operation does *not* match with the substrate symmetry and hence conserves the adsorption site of N only (top site). The B atoms, however, are imaged from an hcp hollow site to an fcc hollow site and vice versa (by both the mirror operation and the 60° rotation).

We finally mention that despite the different adsorption configurations, both B and N lie at the same adsorption height in the two α domains, as illustrated in the vertical true-scale model shown in Fig. 9(b). Hence the adsorption height cannot be the origin of the image contrast we have detected in LEEM for the two α domains. It must rather be a small difference in the chemical interaction that is caused by the different adsorption sites for B. This is in agreement with previous density functional theory (DFT) calculations predicting that (N, B) = (top, fcc) is the energetically most favorable adsorption configuration, with a marginally larger adsorption energy than (N, B) = (top, hcp) [47,48].

IV. CONCLUSIONS

Our combined LEEM and NIXSW investigation of a single hBN layer on a defect-rich Ni(111) surface reveals a clear correlation between the mesoscopic domain structure and the local adsorption geometry that is identified by two independent experiments on two separate *in situ* prepared samples. The high defect density of the Ni(111) surface leads to a pref-

erential nucleation of two epitaxial hBN domains α_1 and α_2 with identical periodicity but different azimuthal orientation. The lattice of one domain is aligned with that of the bulk, and the other is rotated by 60° . Additionally, in LEEM we detected another parasitic type of domain, the β domains, which are not aligned with the substrate but take arbitrary orientations.

The two α domains exhibit different nucleation densities and growth rates and do not cover equal areas of the Ni(111) surface when the hBN layer is complete. This indicates different adsorption energies for the two domains, which in turn is caused by there being different adsorption sites for boron. In an NIXSW experiment performed on the (111) and the (-111) Bragg reflections, we uncovered the adsorption sites: While nitrogen uniquely occupies the on-top site, boron atoms occupy both the fcc hollow and hcp hollow sites. The majority (70% on average for both experiments) of B atoms are found on the fcc hollow sites forming the α_2 domains. Only about 30% of the boron atoms are found on hcp hollow sites in α_1 domains. The different B adsorption sites explain the different azimuthal rotation of the two α domains.

We conclude that the majority domain with a (N,B) = (top, fcc) adsorption site configuration represents the energetically most favorable adsorbate structure for hBN on a

defect-rich Ni(111) surface. The second most frequently observed structure is its 60° -rotated counterpart with a (N, B) = (top, hcp) configuration. Our study hence underlines the crucial role of the atomic adsorption configuration for the mesoscopic domain structures of *in situ* fabricated 2D materials on highly reactive surfaces.

Data shown in the main text are available at the Jülich DATA public repository [49].

ACKNOWLEDGMENTS

M.R., Y.-R.L., and C.K. acknowledge funding by the Deutsche Forschungsgemeinschaft (DFG, German Research Foundation) through SFB 1083, Structure and Dynamics of Internal Interfaces (sub-project A12), and M.A. and B.S. acknowledge funding by the DFG through TRR 173 - 268565370 (projects A02 and B05). B.S. further acknowledges funding by the Dynamics and Topology Center funded by the State of Rhineland Palatinate. We thank the Diamond Light Source for beamtime on I09 under proposal SI18787. We are also very grateful for the support by the I09 beamline staff (T.-L. Lee, P. K. Thakur, D. Duncan, and D. McCue) during the NIXSW experiment.

- [1] Y. P. Feng, L. Shen, M. Yang, A. Wang, M. Zeng, Q. Wu, S. Chintalapati, and C.-R. Chang, Wiley Interdiscip. Rev.: Comput. Mol. Sci. 7, e1313 (2017).
- [2] M. Gobbi, E. Orgiu, and P. Samorì, Adv. Mater. (Weinheim) 30, 1706103 (2018).
- [3] E. C. Ahn, npj 2D Mater. Appl. 4, 17 (2020).
- [4] A. K. Geim and K. S. Novoselov, Nat. Mater. 6, 183 (2007).
- [5] K. V. Emtsev, A. Bostwick, K. Horn, J. Jobst, G. L. Kellogg, L. Ley, J. L. McChesney, T. Ohta, S. A. Reshanov, J. Röhrl, E. Rotenberg, A. K. Schmid, D. Waldmann, H. B. Weber, and T. Seyller, Nat. Mater. 8, 203 (2009).
- [6] C. Busse, P. Lazić, R. Djemour, J. Coraux, T. Gerber, N. Atodiresei, V. Caciuc, R. Brako, A. T. N'Diaye, S. Blügel, J. Zegenhagen, and T. Michely, Phys. Rev. Lett. 107, 036101 (2011).
- [7] F.-f. Zhu, W.-j. Chen, Y. Xu, C.-l. Gao, D.-d. Guan, C.-h. Liu, D. Qian, S.-C. Zhang, and J.-f. Jia, Nat. Mater. 14, 1020 (2015).
- [8] M. Maniraj, B. Stadtmüller, D. Jungkenn, M. Düvel, S. Emmerich, W. Shi, J. Stöckl, L. Lyu, J. Kollamana, Z. Wei, A. Jurenkow, S. Jakobs, B. Yan, S. Steil, M. Cinchetti, S. Mathias, and M. Aeschlimann, Commun. Phys. 2, 12 (2019).
- [9] K. F. Mak, C. Lee, J. Hone, J. Shan, and T. F. Heinz, Phys. Rev. Lett. 105, 136805 (2010).
- [10] T. Cao, G. Wang, W. Han, H. Ye, C. Zhu, J. Shi, Q. Niu, P. Tan, E. Wang, B. Liu, and J. Feng, Nat. Commun. 3, 887 (2012).
- [11] Q. H. Wang, K. Kalantar-Zadeh, A. Kis, J. N. Coleman, and M. S. Strano, Nat. Nanotechnol. 7, 699 (2012).
- [12] K. S. Novoselov, A. K. Geim, S. V. Morozov, D. Jiang, M. I. Katsnelson, I. V. Grigorieva, S. V. Dubonos, and A. A. Firsov, Nature (London) 438, 197 (2005).
- [13] D. Xiao, G.-B. Liu, W. Feng, X. Xu, and W. Yao, Phys. Rev. Lett. 108, 196802 (2012).

- [14] E. Voloshina and Y. Dedkov, Phys. Chem. Chem. Phys. 14, 13502 (2012).
- [15] I. Pletikosić, M. Kralj, P. Pervan, R. Brako, J. Coraux, A. T. N'diaye, C. Busse, and T. Michely, Phys. Rev. Lett. 102, 056808 (2009).
- [16] A. Varykhalov, D. Marchenko, J. Sánchez-Barriga, M. R. Scholz, B. Verberck, B. Trauzettel, T. O. Wehling, C. Carbone, and O. Rader, Phys. Rev. X 2, 041017 (2012).
- [17] C. R. Dean, A. F. Young, I. Meric, C. Lee, L. Wang, S. Sorgenfrei, K. Watanabe, T. Taniguchi, P. Kim, K. L. Shepard, and J. Hone, Nat. Nanotechnol. 5, 722 (2010).
- [18] A. K. Geim and I. V. Grigorieva, Nature (London) 499, 419 (2013).
- [19] M. Xu, T. Liang, M. Shi, and H. Chen, Chem. Rev. (Washingon, DC) 113, 3766 (2013).
- [20] L. Song, L. Ci, H. Lu, P. B. Sorokin, C. Jin, J. Ni, A. G. Kvashnin, D. G. Kvashnin, J. Lou, B. I. Yakobson, and P. M. Ajayan, Nano Lett. 10, 3209 (2010).
- [21] Q. Han, B. Yan, T. Gao, J. Meng, Y. Zhang, Z. Liu, X. Wu, and D. Yu, Small 10, 2293 (2014).
- [22] T. Niu and A. Li, Prog. Surf. Sci. 90, 21 (2015).
- [23] C. Brülke, T. Heepenstrick, I. Krieger, B. Wolff, X. Yang, A. Shamsaddinlou, S. Weiß, F. C. Bocquet, F. S. Tautz, S. Soubatch, and M. Sokolowski, Phys. Rev. B **99**, 121404(R) (2019).
- [24] M. Schaal, T. Aihara, M. Gruenewald, F. Otto, J. Domke, R. Forker, H. Yoshida, and T. Fritz, Beilstein J. Nanotechnol. 11, 1168 (2020).
- [25] W. Auwärter, Surf. Sci. Rep. 74, 1 (2019).
- [26] W. Auwärter, T. J. Kreutz, T. Greber, and J. Osterwalder, Surf. Sci. 429, 229 (1999).

- [27] G. B. Grad, P. Blaha, K. Schwarz, W. Auwärter, and T. Greber, Phys. Rev. B 68, 085404 (2003).
- [28] M. Muntwiler, W. Auwärter, F. Baumberger, M. Hoesch, T. Greber, and J. Osterwalder, Surf. Sci. 472, 125 (2001).
- [29] M. Ohtomo, Y. Yamauchi, X. Sun, A. A. Kuzubov, N. S. Mikhaleva, P. V. Avramov, S. Entani, Y. Matsumoto, H. Naramoto, and S. Sakai, Nanoscale 9, 2369 (2017).
- [30] R. Drost, S. Kezilebieke, M. M. Ervasti, S. K. Hämäläinen, F. Schulz, A. Harju, and P. Liljeroth, Sci. Rep. 5, 16741 (2015).
- [31] P. C. Mende, Q. Gao, A. Ismach, H. Chou, M. Widom, R. Ruoff, L. Colombo, and R. M. Feenstra, Surf. Sci. 659, 31 (2017).
- [32] Y. Yang, Q. Fu, H. Li, M. Wei, J. Xiao, W. Wei, and X. Bao, ACS Nano 9, 11589 (2015).
- [33] W. Auwärter, M. Muntwiler, J. Osterwalder, and T. Greber, Surf. Sci. 545, L735 (2003).
- [34] D. Woodruff, Rep. Prog. Phys. 68, 743 (2005).
- [35] J. Zegenhagen, Surf. Sci. Rep. 18, 202 (1993).
- [36] G. van Straaten, M. Franke, F. C. Bocquet, F. S. Tautz, and C. Kumpf, J. Electron Spectrosc. Relat. Phenom. 222, 106 (2018).
- [37] J. Felter, M. Raths, M. Franke, and C. Kumpf, 2D Mater. 6, 045005 (2019).
- [38] A. B. Preobrajenski, A. S. Vinogradov, and N. Mårtensson, Phys. Rev. B 70, 165404 (2004).
- [39] P. Bachmann, F. Düll, F. Späth, U. Bauer, H.-P. Steinrück, and C. Papp, J. Chem. Phys. 149, 164709 (2018).
- [40] N. Fairley, CasaXPS, version 2.3.19PR1.0, Casa Software, Teignmouth, UK.

- [41] F. C. Bocquet, G. Mercurio, M. Franke, G. van Straaten, S. Weiß, S. Soubatch, C. Kumpf, and F. S. Tautz, Comput. Phys. Commun. 235, 502 (2019).
- [42] TORRICELLI is a XSW data analysis and simulation program written by F.C. Bocquet, G. Mercurio *et al.* [41]. The latest version of the open-source software is available at https://www.fz-juelich.de/torricelli/EN/Home/home_node.html.
- [43] Y. Gamo, A. Nagashima, M. Wakabayashi, M. Terai, and C. Oshima, Surf. Sci. 374, 61 (1997).
- [44] F. H. Farwick zum Hagen, D. M. Zimmermann, C. C. Silva, C. Schlueter, N. Atodiresei, W. Jolie, A. J. Martinez-Galera, D. Dombrowski, U. A. Schröder, M. Will, P. Lazić, V. Caciuc, S. Blügel, T.-L. Lee, T. Michely, and C. Busse, ACS Nano 10, 11012 (2016).
- [45] M. Schwarz, A. Riss, M. Garnica, J. Ducke, P. S. Deimel, D. A. Duncan, P. K. Thakur, T.-L. Lee, A. P. Seitsonen, J. V. Barth, F. Allegretti, and W. Auwärter, ACS Nano 11, 9151 (2017).
- [46] C. Brülke, T. Heepenstrick, N. Humberg, I. Krieger, M. Sokolowski, S. Weiß, F. S. Tautz, and S. Soubatch, J. Phys. Chem. C 121, 23964 (2017).
- [47] A. N. Y. Gamou, M. Terai, and C. Oshima, Sci. Rep. Res. Inst., Tohoku Univ., Ser. A 44, 211 (1997).
- [48] M. N. Huda and L. Kleinman, Phys. Rev. B 74, 075418 (2006).
- [49] M. Raths et al., data used in: Growth, domain structure, and atomic adsorption sites of hBN on the Ni(111) surface. Jülich DATA (2021), https://doi.org/10.26165/JUELICH-DATA/QMS0VG.